Lab on a Chip

Thermographic Characterization of Ultra-thin Liquid Films Formation and Evaporation in Microchannels

Journal:	*Lab on a Chip*
Manuscript ID	LC-ART-04-2019-000301.R1
Article Type:	Paper
Date Submitted by the Author:	13-Jun-2019
Complete List of Authors:	Habibi Matin, Meisam; University of Florida Fazeli, Abdolreza; University of Florida Moghaddam, Saeed; University of Florida, ;

SCHOLARONE™
Manuscripts

Lab on a Chip

Thermographic Characterization of Thin Liquid Films Formation and Evaporation in Microchannels

Meisam Habibi Matin[a], Abdolreza Fazeli [a] and Saeed Moghaddam*,[a]

The science of transport in microchannels has greatly benefited applications ranging from micro-mixing, chemical synthesis and biological analysis to compact and efficient energy devices. One of the most critical and intricate phenomena in this field of science is the dynamics of thin liquid films formation during the flow of liquid and gas/vapor mixture. These films can form in microseconds and be less than a micrometer thick, while dominating thermal transport in phase-change process. Here, we report capturing details of this phenomena using a new measurement technique with unprecedented spatial and temporal resolutions of 20 μm and 100 μs, respectively. Thin films with thicknesses ranging from 1 to 20 μm forming around elongated bubbles over a capillary number range of 0.025 to 0.1 are characterized. The measurements suggest that these films thermally develop and evaporate at timescales on the order of 1-10 ms, two orders of magnitude longer than their formation timescale. The formation, reflow and evaporation of the liquid film constitute a complex dynamic involving variations of the film thickness over the periphery of a rectangular channel, leading to a thicker liquid film feeding (through lateral capillary wicking) a much thinner rapidly evaporating film. As a result, the thinner film dictates the rate of surface heat transfer while the thicker film determines the duration of thin film evaporation. A modified Bretherton model provides the best fit to the experimental results.

1. Introduction

Microfluidics have greatly benefited fundamental and applied research in different fields such as chemistry, biology, and energy[1–5]. The impact of physics of scale on balance of forces, reduced diffusion timescale, enhanced surface area per volume, and improved mixing between the phases are among the factors that have enabled unique performance characteristics in microfluidics[6–9]. One of the most intricate phenomena in this field of science is formation of thin liquid films in multiphase microfluidics[10]. Thin films can form in coaxial flow of low and high viscosity fluids (e.g. a gas and a liquid) in a channel. Formation of these films has been studied to influence transport of microorganisms through unsaturated porous media[11], to detach bacteria from confined microgeometries[12] and to understand mucus transport in lung airways[13]. Thin liquid films play a prominent role in two-phase microreactors[14,15] and cooling surfaces using microchannel heat sinks[16,17]. For example, in electronics cooling and advance evaporator heat exchangers, thin films dictate the heat transfer coefficient[18,19]. However, formation and evaporation of thin films in microchannels have not been experimentally characterized despite nearly two decades of studies.

These films can be on the order of a micrometer thick, form in microseconds, and flow, become unstable and rupture/atomize during transition from one flow regime to another. Hydrodynamics of thin films formation is a generic phenomenon that underpins applications well beyond microfluidics, such as thin-film coating[20]

and gas-assisted manufacturing in plastic molding[21]. Characterization of these films has garnered significant attention for many years, since the pioneering work of Fairbrother and Stubbs[22] and Taylor[23]. Theoretical studies were later conducted to relate the liquid film profile to the fluid and flow properties[24–27]. The proposed correlations have often been developed for a simplified case of steady state, fully developed and 1D liquid-vapor interface in a channel with a round cross section; conditions that are rarely satisfied in microfluidic devices.

The experimental measurement of liquid films thickness has been conducted using optical techniques[28–30] in adiabatic conditions. Techniques such as laser confocal displacement (LCDM)[31] and planar laser-induced fluorescence (PLIF)[30] involve assumptions and correction factors to account for variations in refractive index of materials and curvature of interfaces. Considering different factors responsible for measurement uncertainties, the capabilities of optical techniques become limited in the 1-10 μm film thickness range[29,31,32]. Furthermore, complexities associated with optical access to liquid-vapor interfaces along the periphery of non-circular, often opaque, microchannels under highly transient conditions have made experimental characterization of thin films under realistic thermo-hydrodynamic conditions extremely challenging.

In this work, a thermal-based technique is utilized to determine the thickness of liquid films formed around microbubbles during boiling in a rectangular microchannel with a 300×75 μm² cross-section, and a length of 25 mm. The approach involves the implementation of a sensor array capable of resolving temperature and heat flux at the microchannel wall and fluid interface. While measurement of the

[a.] Department of Mechanical and Aerospace Engineering, University of Florida, Gainesville, FL 32611, USA
* Corresponding author: Prof. Saeed Moghaddam; email: saeedmog@ufl.edu

Please do not adjust margins
Lab on a Chip
Page 2 of 9

wall temperature is trivial and has been accomplished using microfabricated sensors[33,34], measurement of the wall heat flux has been a challenge.

2. Experimental setup

2.1. Sensor design concept

The difficulty in measuring surface heat flux arises from the conjugate nature of heat transfer at the wall-fluid interface, as rapid changes in wall boundary conditions (e.g. transition from flow of a liquid slug to formation of thin liquid films) leads to rapid heat diffusion within the heated wall. Hence, the actual heat flux crossing the wall-liquid interface remains unknown. Two strategies implemented to limit heat transfer within the microchannel wall are 1) microfabrication of an extremely thin wall microchannel suspended between the fluid inlet and outlet[33] and 2) use of a glass substrate with substantially lower thermal conductivity relative to typical boiling surfaces[34,35]. However, these studies still indicated substantial heat transfer within the wall resulting in unknown heat flux at the wall-liquid interface.

To help describe intricacies associated with this phenomenon and introduce the technique implemented in this study, numerical simulations have been conducted to illustrate the effect of substrate material properties on measurements spatial and temporal resolutions. Fig. 1A depicts a quartz substrate (used by Basu et al.[34] and Rao et al.[35]) subjected to a sudden rise in the heat transfer coefficient associated with formation of a thin liquid film following the flow of a liquid slug over a 300-μm-wide area at the middle of the substrate. As the temperature contours indicate, this event results in temperature drop across the substrate, triggering inflow of an unknown amount of heat from the neighbouring regions. This process not only couples the surface heat transfer event to other neighboring events but also engages the entire thermal mass of the impacted zone with the change occurred at the surface-liquid interface, resulting in a slow response to changes in boundary conditions (on the order of 100 ms[34,35]).

A composite wall utilized in this study (Fig. 1B), consisting of a microscale (10-μm-thick) SU8 polymer layer (with a negligible thermal mass) coated on a high thermal conductivity substrate (silicon for FC-72 liquid tests), overcomes this issue. Under the sudden change in boundary conditions described above, temperature of the SU8-liquid interface 20 μm away from the region subjected to variations in boundary conditions experiences a temperature change less than the measurement accuracy of the sensors. This implies that the spatial resolution of the sensors is 20 μm. Evidently, this resolution can be further enhanced by reducing the SU8 layer thickness. Since the temperature variation is restricted to a small material volume, sensors' response time is very short (~100 μs), as will be shown in section 3.1.

Measurement of the temperature of the two sides of the SU-8 layer enables calculation of the local heat flux through either using a numerical model of the SU-8 layer or $q'' = k\Delta T/\delta_{su8}$, where ΔT is
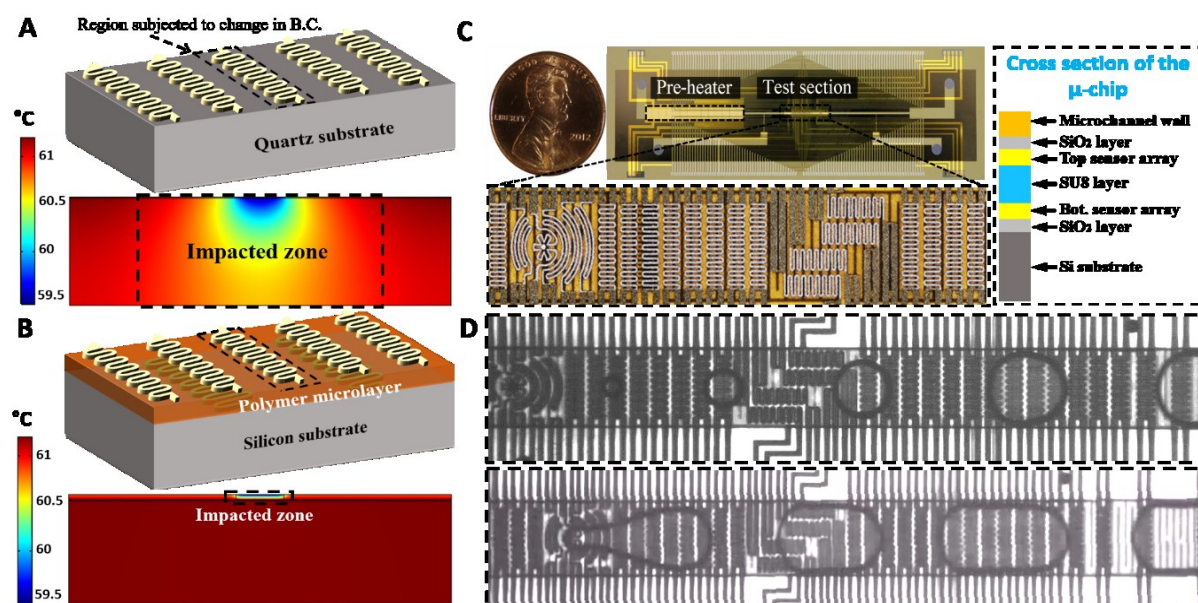

Fig. 1. A. Typical single layer sensor design on a quartz substrate and associated numerical temperature distribution, B. Composite wall design implemented in this study and associated numerical temperature distribution. The simulated area is 2400×600 μm². Thickness of the polymer layer (SU-8) on the composite wall is 10 μm. The main substrate (quartz or silicon) is heated by a 0.5-μm-thick heater layer installed on its top surface. The interface is initially subjected to a convective heat transfer coefficient 2000 W/m²K that corresponds to a single phase flow. A 300-μm-wide area at the centre of the substrate is suddenly exposed to a heat transfer coefficient of 20,000 W/m²K (for a period of 8 ms) associated with evaporation of a thin liquid film. C. Images of the microfluidic chip (top left), sensor array (bottom left) and cross-sectional view of the chip (right). D. Bubbles generated at frequency of 140 Hz and pulsed voltage amplitudes of 0.2 V (top) and 0.4 V (bottom).

the temperature difference across the polymer layer and δ_{su8} is thickness of the polymer layer. The high thermal conductivity of the substrate ensures normal flow of heat within the substrate, as in the case of a typical boiling surface material.

2.2. Fabrication of the microfluidic chip

The microfluidic chip was fabricated on a 500-μm-thick silicon wafer through a multistep microfabrication process. A total of 50 resistance temperature detectors (RTDs) consisting of a 50-nm-thick Titanium adhesion layer and a 100-nm-thick Platinum layer were fabricated at the Si-SU8 and SU8-fluid interfaces. Each sensor is 50 μm wide and placed 15 μm apart from its neighboring sensor. The chip was equipped with a microfabricated pre-heater section made to heat the working fluid, FC-72 (3M™ Fluorinert™), to a desired temperature before entering the test section. The liquid temperature was measured after the pre-heater section by a single RTD sensor positioned between the pre-heater and test section.

To control the nucleation site, a 300 nm in diameter cavity was fabricated using a focused ion beam (FIB) milling machine. The cavity was surrounded by a pulsed function microheater fabricated on the SU8 film. To increase the temperature measurements accuracy, a 4-wire configuration, also referred to as a Kelvin connection, was utilized. The microfluidic chip was wire bonded to a custom made, double-sided printed circuit board connected to a high-speed data acquisition system. Images of the microfluidic chip, sensor array and bubbles generated at a frequency of 140 Hz are presented in Figs. 1C & D. The test device fabrication process is discussed in details in the ESI[†].

2.3. Test loop and data collection

Fig. 2 depicts the experimental setup. Since each RTD sensor has four connections (excitation +/- and channel amplifier +/-), all similar connections of all sensors are directed to a separate ribbon socket and routed to a data acquisition (DAQ) system. The DAQ system, which consists of a current excitation module (NI SCXI-1581), a channel amplifier module (i.e., signal conditioning module) (NI SCXI-1120C), a high speed DAQ module (NI PXI-6289), and a programmable dc power supply module (NI PXI-4110), is commanded by an embedded controller (NI PXI-8115). The temperature data are recorded at a frequency of 20 kHz. The pulsed function microheater is connected to the programmable dc power supply module. All data collection, as well as the control for the applied dc voltage of the pulsed function microheater, is performed using a LabVIEW program.

2.4. Sensor calibration and uncertainty analysis

The RTD sensors are calibrated prior to the flow boiling experiments to obtain the voltage-temperature relationship of each sensor. The calibration tests are done in a uniform temperature oven for a temperature range of 40°C to 90°C. A constant current excitation of 100 μA is supplied to each sensor. The temperature sensors have negligible self-heating. The obtained voltage-temperature curves

show a linear trend and the sensitivity of the RTD sensors, the slope of the V-T curves, is 0.13 mV/°C. The data acquisition system has a maximum uncertainty of ±28 μV, at a gain of 100 with a minimum detectable voltage change of 1 μV. Considering the sensitivity of the sensors and the voltage uncertainty, the maximum error in temperature measurements is determined to be ±0.25°C. In addition, the maximum uncertainty in the measurement of the SU8 film thickness and the local heat flux data are ±0.01 μm and ±1 W/cm^2, respectively.
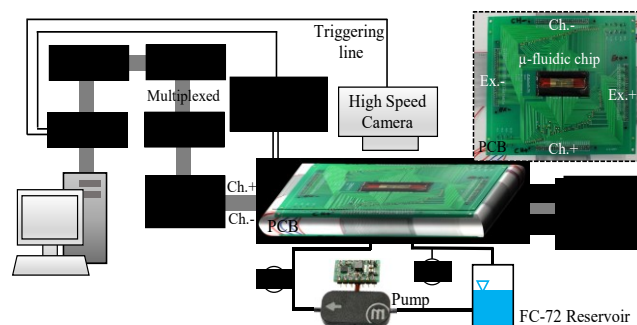

Fig. 2. Schematic of the experimental setup.

3. Results and discussion

In a typical experiment, single bubbles are generated at a desired rate and size by adjusting the frequency and amplitude of the voltage applied to the pulsed function microheater surrounding the nucleation site. The bubble length and velocity vary depending on the surface temperature and mass flux. As a bubble moves along the microchannel (Figs. 3A-E), sensors measure the surface temperature and heat flux. Figs. 3F and G provide surface heat flux and temperature results, respectively, recorded by sensor 35 as the bubble passes through the microchannel (note that time zero is arbitrary). Comprehensive discussions on mechanisms responsible for variations of surface temperature and heat flux (thin film evaporation, partial dry-out, transient conduction, and micro-convection) are provided in our prior studies [36,37]. Here, the thin film evaporation process is briefly discussed to set the stage for describing the method used to determine the film thickness using the surface temperature and heat flux data. The thin film evaporation mode of heat transfer initiates as the leading edge of the bubble arrives at the sensor (point *A* marked on Fig. 3F), triggering a sudden rise in the surface heat flux. This abrupt change in heat flux is due to rapid evaporation of the liquid film. Following an initial spike (event *A-B*), the local heat flux remains relatively constant for a period of time (event *B-C*). After this period, heat flux starts to decline and eventually diminishes as the liquid film mostly evaporates, and the surface experiences dryout (event *D-E*). This process of thin film formation and evaporation finally ends when the trailing edge of the bubble arrives over the sensor, and rewets the surface. This rewetting of the surface by a relatively cooler liquid triggers a quick rise in the surface heat flux (point *E*). After this rapid quenching
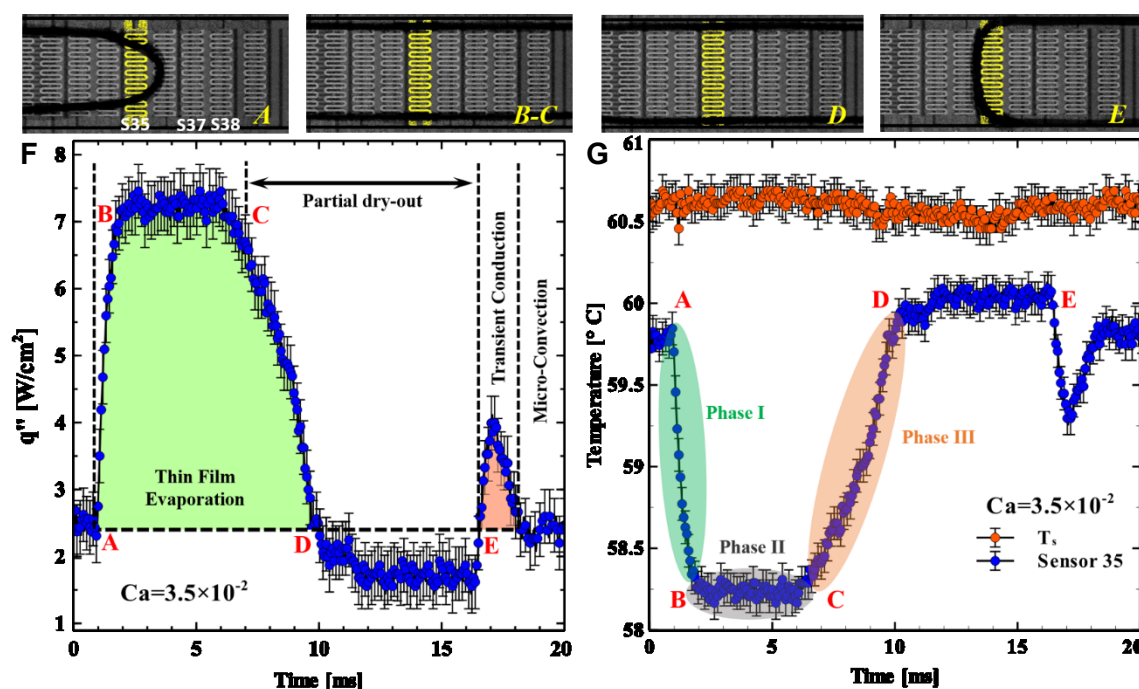
Fig. 3. Data recorded by the high speed camera and sensor S35 (highlighted), A. Bubble's tip passing over the sensor causing thin film formation, B-C. Steady thin film presence over the sensor, D. Partial dryout initiated on the sensor, E. Bubble's tale passing over the sensor, F. Local heat flux values and heat transfer mechanisms associated with the moving bubble over sensor 35, G. Temperature values recorded as a function of time highlighting three distinct phases associated with the thin film heat transfer mode.

effect, the local heat flux declines to the level before the formation of the thin film (i.e. point *A*).

3.1. Thermohydraulics of the thin film evaporation process

The experimental results (Fig. 3) suggest that the thin film evaporation process consists of the following three phases:

Phase I: the bubble front has reached the sensor and caused a significant increase in the surface heat flux as well as a sudden drop in surface temperature.

Phase II: the surface temperature reached its minimum value, a quasi-steady condition started during which temperature and heat flux remained constant for a short period of time.

Phase III: as the liquid film dried out, the surface temperature gradually increased until it reached its maximum value.

In the following, we utilize the experimental data recorded in individual phases to explain different stages associated with formation, development and evaporation of the liquid layer and characterize its heat & mass transport properties.

Phase I: formation and thermal development of thin film

The bubble images (Fig. 3A-E) show that the tip of the bubble moves at a velocity of ~1 m/s. At this speed, it takes approximately 50 μs for it to pass over Sensor 35 and form the liquid film (with a thickness of δ_0). This time period is two orders of magnitude shorter than the evaporation time of the liquid film (~10 ms). Hence, the amount of heat transferred into the liquid film that could have caused change in its thickness (due to evaporation) is considered negligible.

After the liquid film has formed, it starts to thermally develop until reaching the quasi-steady condition (i.e. point *B* in Figs. 3F & G). The initial temperature of the film can be readily determined using the surface temperature and heat flux data. The temperature profile within the film is that of a few microns thick layer of liquid carved from the liquid slug present on the surface before the film formation. This temperature profile is assumed to be linear $T(y) = T_s - q''\delta(y)/k$, as correctly done by Thome et al.[19]. This is further validated below. The next step in analyzing the film is to determine its initial thickness (δ_0). δ_0 can be calculated from δ_{Ph-II} (i.e. thickness of the liquid layer at the onset of Phase II) as follows

$$\delta_0 = \delta_{Ph-II} + \Delta\delta_{Ph-I} \qquad (1)$$

Since the film in Phase II has reached a fully developed temperature profile, its thickness can be readily calculated using the surface temperature and heat flux values ($\delta_{Ph-II} = k\Delta T/q''$, where $\Delta T = T_s - T_{sat}$). $\Delta\delta_{Ph-I}$ can then be estimated using the energy balance equation $\Delta\delta_{Ph-I} = \int_0^{t_B}(q''/\rho h_{fg})dt$, with h_{fg} being the latent heat of vaporization. Using the heat flux data (Fig. 3F), δ_{Ph-II} and $\Delta\delta_{Ph-I}$ are calculated to be 1.9 μm and 0.25 μm, respectively.

To validate the procedure discussed above, a set of numerical simulations was conducted and the results were compared with the experimental data in Fig. 4A. The comparison shows a match between the experimental and numerical data. Specifically, the experimental temperature follows the numerical prediction with a maximum temporal deviation of ~100 μs in the middle of Phase I, representing an unprecedented temporal resolution of the temperature sensors. The numerical results for temperature profile within the FC-72 and SU-8 films as a function of time are provided in

Fig. 4B. Evidently, it takes 1 ms for the temperature profile to become fully developed. Variation of the liquid layer thickness was also captured using this method (Fig. 4B inset) that agreed well with the estimated value. Details of numerical solution are provided in the ESI†.
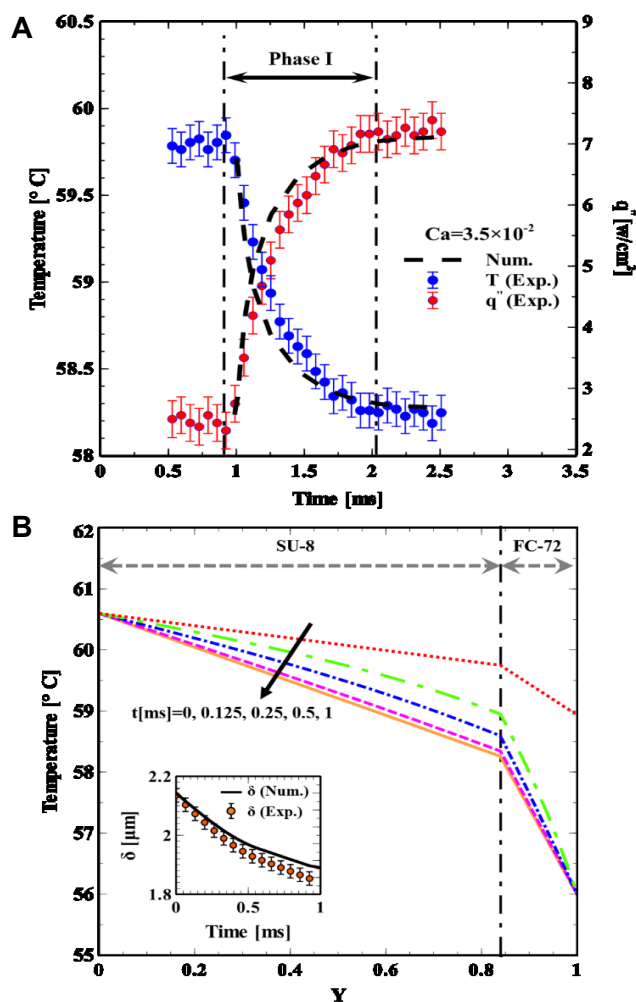

Fig. 4. Comparison between simulation results and experimental data: A. The experimental values for surface temperature and heat flux as a function of time are accurately predicted using a numerical simulation that considers the effect of liquid evaporation and transient conduction, B. Temperature profile in FC-72 domain changes with time to reach steady state condition ($Y = y/[\delta_{SU8} + \delta_{FC-72}(t)]$), Inset compares the numerical and experimental changes in liquid film thickness.

Phase II: quasi-steady thin film evaporation

The Phase II process initiated as the temperature profile in the liquid layer reached its quasi-steady state (cf. Fig. 3G). The surface temperature and heat flux leveled out for several milliseconds. The relatively constant heat flux and surface temperature observed in this phase implies that the liquid film thickness should also remain constant ($\delta_{Ph-II} = k(T_s - T_{sat.})/q''$). Therefore, liquid must have been continuously delivered to the heated area to compensate for the evaporation caused by the

applied heat flux ($\dot{m}_{delivered} = \dot{m}_{evap.} = q''/\dot{m}h_{fg}$). There could be only two paths for the liquid around the bubble to feed the evaporating liquid film. Fig. 5 depicts these paths:

$$\dot{m}_{delivered} = \dot{m}_{w,f} + \dot{m}_{w,s} \qquad (2)$$

where $\dot{m}_{w,f}$ and $\dot{m}_{w,s}$ represent liquid wicking due to the capillary pressure generated on front and sides of the bubble, respectively. In capillary driven flows, the change in radius of curvature at the liquid-vapor interface in any direction, generates a capillary pressure ($P_c = \sigma \times \delta''/[1 + \delta'^2]^{3/2}$, δ denotes the liquid layer thickness), which induces the liquid flow in that direction ($\dot{m}_{w,f} = \frac{\rho}{\mu} \times \frac{dP_c}{dx} \times \frac{\delta^3}{3}$ and $\dot{m}_{w,s} = \frac{\rho}{\mu} \times \frac{dP_c}{dz} \times \frac{\delta^3}{3}$). More details are provided in the ESI†. To estimate the capillary-driven mass flux in the flow direction ($\dot{m}_{w,f}$), the capillary pressure gradient was first calculated using the directional derivatives of thin film thickness (i.e. $d\delta/dx$ & $d^2\delta/dx^2$). Figure 6A plots the liquid layer thickness on three consecutive sensors calculated as a function of time using the experimental data. Evidently, there was no noticeable variation in thickness of the liquid layer in the flow direction, implying that the slope ($d\delta/dx \cong [\delta_i - \delta_{i-1}]/\Delta x$) and curvature ($d^2\delta/dx^2 \cong [\delta_{i+1} - 2\delta_i + \delta_{i-1}]/\Delta x^2$) of the meniscus over the width of three sensors (~350 μm) were almost zero. The contribution of the capillary driven liquid flow from the front side of the bubble was determined to be insignificant ($\dot{m}_{w,f} \sim 0$).
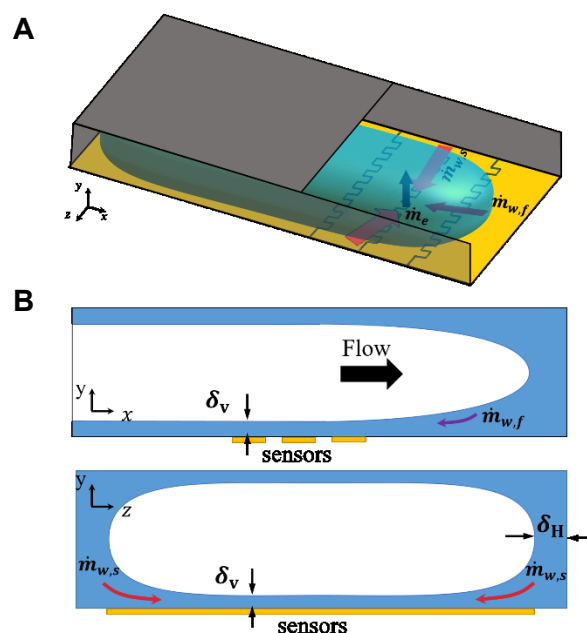

Fig. 5. Liquid delivery to the heated area during the Phase II: A. 3D & B. 2D schematics illustrating different mechanisms of liquid delivery to the heated surface.

Hence, for the liquid film thickness to remain constant, the transversal wicking mass flux ($\dot{m}_{w,s}$) must be responsible for replenishing the liquid film. A closer look at the bubble images (Figs. 3A-E) clearly shows that the thickness of a body of liquid left at the sides of the bubble continuously declines indicating the flow of liquid
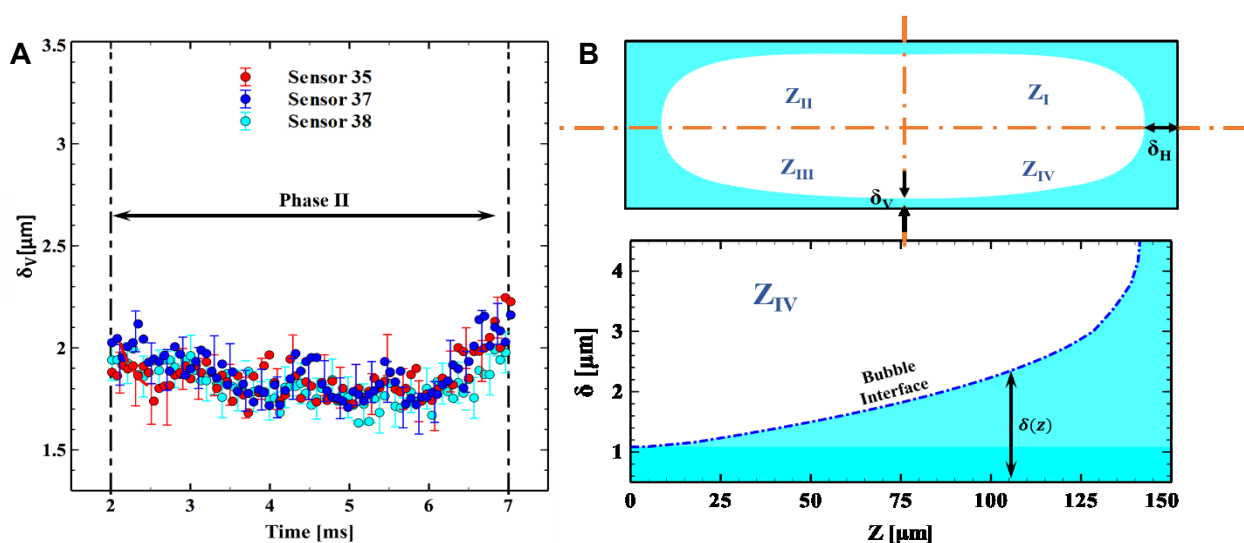
Please do not adjust margins
Lab on a Chip
Page 6 of 9

Fig. 6. A. Film thickness (δ_V) measured experimentally, remains constant spatially and temporally during Phase II in the flow direction, B. Bubble cross-sectional (not to scale) reconstructed using simulations results.

in the z-direction (Fig. 6B). The mass balance equation for the evaporating liquid film is then reformulated as:

$$\dot{m}_{evap.} - \dot{m}_{w,s} \cong 0 \tag{3}$$

$\dot{m}_{evap.}$ and $\dot{m}_{w,s}$ are defined as $\dot{m}_{evap.}(z) = k_f \Delta T \times W / h_{fg} \times 1/\delta(z)$ and $\dot{m}_{w,s}(z) = \rho/\mu \times dP_c/dz \times W \times \delta(z)^3$, where W denotes the sensor width. To solve this equation, a liquid film with the general form of $\delta(z) = \sum_{n=0}^{5} C_n (z/L)^n + A \times (1 - z/L)^k$ is assumed over the width of the microchannel such that it satisfies the mass balance equation (Eq. 3). The solution to this problem provides the shape of the liquid profile in the transversal direction, as depicted in Fig. 6B (details provided in the ESI†).

Phase III: termination of thin film evaporation

The final phase in the thin film evaporation process begins as the available liquid on the sides of the bubble diminishes and the surface partially dries out. At this condition, the capillary driven flow could no longer compensate for the evaporating liquid ($\dot{m}_s < \dot{m}_{evap.}$) and surface of the sensor starts to dry out. The vapor, now directly in contact with the surface, acts as a thermal insulator ($k_{FC-72,vapor} \ll k_{FC-72,liquid}$), resulting in an increase in surface temperature.

3.2. Magnitude and variations of thin film thickness

The method described in the previous section was utilized to determine the liquid film thickness at different test conditions. Fig. 6A depicts the results for film thickness along the channel minor (δ_V) and major (δ_H) axes. The results indicated that δ_H changes from 10 µm to 24 µm (showed on the left y-axis) while δ_V changes only slightly (showed on the right y-axis) when capillary number (i.e. $Ca = \mu U/\sigma$; U: bubble velocity) is increased from 0.025 to 0.1. Fig. 7A provides a manifestation of the impact of this liquid film distribution on the surface heat flux. This figure illustrates the temporal variations of the surface heat flux at different flow conditions (i.e. bubble velocities), Ca numbers of 0.0325 and 0.065, at a constant

surface temperature (T_s=60°C). The data shows that the maximum heat flux is almost identical for both cases. This indicates a similar δ_V, since it is the film thickness over the heated wall that dictates the heat flux (i.e. $q'' \cong k_f \Delta T / \delta_V$). The thicker liquid layer formed at the sides of the bubble along the major channel axis (δ_H) determines the overall evaporation time ($\delta t_{evap.} \propto q'' / [\rho \times h_{fg} \times \delta_H]$), since it feeds the thin liquid layer. Evidently, the longer evaporation time observed in the case of faster moving bubble (i.e. higher Ca) corresponds to a thicker δ_H. This finding shows that in microchannels with a rectangular cross-section, each of the film thicknesses (δ_V and δ_H) plays a significant role in cooling performance of the device. The heat transfer coefficient is dictated by the thin liquid film thickness, δ_V, whereas the overall heat transfer and dryout threshold are dictated by the thick liquid film thickness, δ_H. In prior studies[18,19], since characterization of the liquid films in rectangular channels was not possible, the average film thickness or the thickness obtained for circular or parallel plate channels have been used to determine the heat transfer performance.

3.3. Comparison with the existing models

Development of models relating the liquid film thickness around a bubble to Ca dates back to several decades ago[24–27,38,39]; notably, to the pioneering work of Bretherton[24] who related the liquid film thickness to the capillary number as $\delta/R = 1.34 Ca^{2/3}$ for $Ca < 0.01$ using planar lubrication equation (i.e. a balance between the viscous force and pressure gradient along the dynamic meniscus). The green dash line in Fig. 7B represents Bretherton's prediction of the liquid film thickness. The channel hydrodynamic diameter is used here to determine the film thickness since the Bretherton model is derived for a 2D axisymmetric (i.e. circular) channel cross-section geometry. Bretherton's[24] assumption of a negligible liquid film thickness relative to the channel diameter ($\delta \ll R$) limited the range of his equation. To extend the model to high capillary number values,
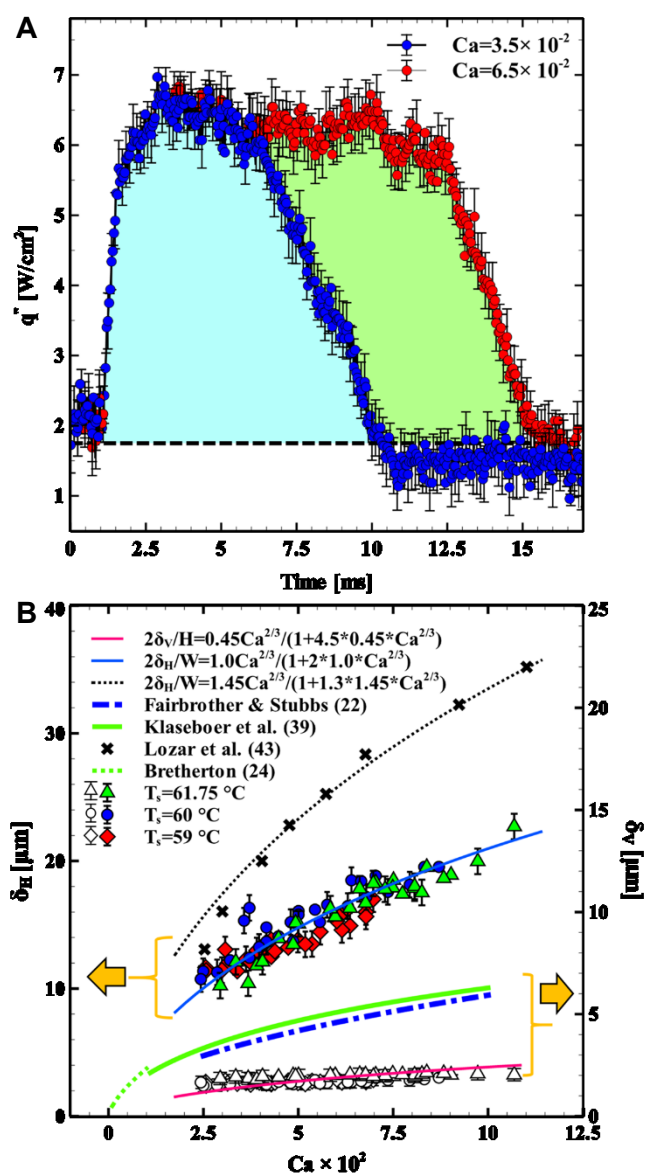
Fig. 7. A. Surface heat flux as a function of Ca number at T_s=60°C. B. Variation of liquid film thickness underneath (δ_v) and around (δ_H) the bubble as a function of Ca number and surface temperature.

Aussillous and Quere [38] replaced R in the Bretherton equation with $R - \delta$ to accurately account for the Laplace pressure, as the meniscus radius decreases with increasing δ. Aussillous and Quere [38] determined $\delta/R = 1.34Ca^{2/3}/(1 + P{\times}1.34Ca^{2/3})$ to be in good agreement with the experimental results of Taylor[23] for Ca values up to 2 at $P = 2.5$. More recently, Klaseboer et al.[39] justified the use of P analytically and determined its value to be 2.79. The green line in Fig. 7B represents the results of this modified Bretherton model[39]. Evidently, the modified Bretherton model predicts thickness of neither one of the films (δ_V and δ_H); highlighting the fact that the hydraulic diameter is not a suitable length scale in determining the liquid film thickness in a channel with a non-circular cross-section.

Hence, Bretherton and similar models[25–27,38–40] that are developed based on the axisymmetric assumption are not suitable for use in flow boiling in microchannels, which are rarely made with a circular cross-section.

Intuitively, confinement in a rectangular channel squeezes a bubble into a non-axisymmetric cross-section shape while surface tension force acts to restore the vapor-liquid interface to the axisymmetric state. Hence, increasing the channel aspect ratio (α) results in thickening of the liquid film along the channel long semi-axis (δ_H), while squeezing the liquid film along the channel short semi-axis (δ_v). A body of fluid dynamics literature concerning adiabatic propagation of air fingers into rectangular tubes filled with a liquid provides valuable insight into physics of liquid films formation on periphery of rectangular cross-section channels. In complementary numerical simulations, Hazel and Heil [41] and De Lozar et al. [42] showed that as Ca increases, the fluid film thickens and in near-square channels the ultimate finger shape becomes axisymmetric at sufficiently high Ca. However, axisymmetric configurations are possible for $\alpha < 2.04$ but never occurs for $\alpha > 2.04$ [41,42]. Instead, the equilibrium finger shape consists of end regions of constant curvature connected by liquid films along the longer side of the channel (details for $Ca = 1.0$ and $\alpha = 3, 7$ are provided). Hazel and Heil [41] further demonstrated that at sufficiently low capillary numbers changes in δ_v with capillary is significantly small relative to changes in δ_H.

In investigating the viscous fingering flow of air into silicone oil, De Lozar et al.[43] determined δ_H in rectangular macrochannels with different aspect ratios. Their results for a channel with an aspect ratio of α=4 (cf. Fig. 7B) are compared with the present experimental data for δ_H. The curve fit to their results renders $2\delta_H/W = 1.45Ca^{2/3}/(1 + 1.3{\times}1.45Ca^{2/3})$ that substantially overestimates the present experimental data. The rate of change in the liquid film thickness in the present data follows $\sim Ca^{2/3}$, with the best fits achieved (cf. Fig. 7B) with $2\delta_H/W = 1.0Ca^{2/3}/(1 + 2 \times 1.0Ca^{2/3})$ & $2\delta_v/H = 0.45Ca^{2/3}/(1 + 4.5 \times 0.45Ca^{2/3})$. Evidently, in the presented correlations, each film thickness is normalized by its corresponding channel dimension (i.e. δ_H/W and δ_v/H). This implies that the interface meniscus curvature associated with the short and long semi-axes, and consequently the capillary forces (which dictates the balance with the viscous forces), are independent of each other. We believe that De Lozar et al.[42] numerical results confirm this independence. De Lozar et al. [42] simulations suggest that pressure difference across the tip of a finger decreases with the channel aspect ratio such that little variations occur when α approaches 4 and the difference for α =7 and α =8 is almost indistinguishable. In other words, at high enough α, the curvature at the tip (which determines the pressure difference) is dominated by the curvature across the channel (of order $1/H$). In the literature, $2\delta_H/W$ is used to characterize the film thickness along the long-axis in high aspect ratio channels. This quantity widely appears in 2D models (i.e. Saffman-Taylor regime) and has been easy to determine experimentally by measuring the finger width ($W - 2\delta_H$).

While a clear explanation for variations of the proportionality constant in $\delta \sim Ca^{2/3}$ remains elusive, and outside the scope of this

study, we wish to highlight a fundamental assumption in Bretherton's[24] and subsequent studies as a potential source of discrepancies. In solving the lubrication equation ($\partial p/\partial x = \mu \, \partial^2 u/\partial r^2$) or balancing the viscous force with the pressure gradient, Bretherton[24] had to assume a shape for the bubble. As such, the liquid-vapor interface region was divided into three segments; a spherical cap, a flat film region and a transition region in between. In writing a balance between the viscous force and the pressure gradient in the transitional region ($\mu u/\delta^2 \sim \sigma/_r/\lambda$), the transition region length (λ) was required. This unknown was estimated by requiring continuity of Laplace pressure at the interface or, in other words, that the curvature of the spherical segment matches the curvature at the end of the transition region. Bretherton[24] assumption of a parabolic profile between the assumed spherical tip and the flat thin film led to the constant in his correlation. Changing these assumptions results in a different constant. For instance, Wong et al.[26] presented an equation in the form of $\delta \sim (Cos\emptyset Ca)^{2/3}$ to account for the effect of contact angle ($\emptyset$) that was assumed to be zero by Bretherton[24].

4. Conclusion

Capability of a sensing technique in characterizing thermohydraulics of thin rapidly forming/evaporating liquid films in multiphase flow in microchannels was demonstrated. The composite structure of the substrate; a thick silicon layer with a low-conductivity overlaying polymer layer, limited temperature variations within the substrate (i.e. impacted zone) to the polymer microlayer resulting in a response time necessary for observation of the thin film formation and evaporation process. Using the temperature and heat flux measurements, and energy and mass conservations, the film thickness along the short and long axes of a rectangular microchannel were determined. The measurements featured inability of the existing correlations in predicting the experimental results. This advancement in measurement capability facilitates modeling of transport in multiphase microchannels, and particularly heat transfer in microchannels flow boiling process in which thin film evaporation process plays a prominent role.

Conflict of Interest

There is no conflicts of interest to declare.

Reference

1 H. A. Stone, A. D. Stroock and A. Ajdari, *Annu. Rev. Fluid Mech.*, 2004, **36**, 381–411.
2 A. Günther and K. F. Jensen, *Lab Chip*, 2006, **6**, 1487–1503.
3 T. M. Squires and S. R. Quake, *Rev. Mod. Phys.*, 2005, **77**, 977–1026.
4 H. Song, D. L. Chen and R. F. Ismagilov, *Angew. Chemie - Int. Ed.*, 2006, 45, 7336–7356.
5 J. R. Thome, *Encyclopedia of Two-Phase Heat Transfer and Flow I*, WORLD SCIENTIFIC, 2015.
6 K. S. Elvira, X. Casadevall i Solvas, R. C. R. Wootton and A. J. de Mello, *Nat. Chem.*, 2013, **5**, 905–915.
7 M. Joanicot and A. Ajdari, *Science (80-.).*, 2005, **309**, 887–888.
8 G. M. Whitesides, *Nature*, 2006, **442**, 368–373.
9 M. Prakash and N. Gershenfeld, *Science (80-.).*, 2007, **315**, 832–835.
10 S. A. Setu, R. P. A. Dullens, A. Hernández-Machado, I. Pagonabarraga, D. G. A. L. Aarts and R. Ledesma-Aguilar, *Nat. Commun.*, 2015, **6**, 1–8.
11 J. Wan, J. L. Wilson and T. L. Kieft, 1994, **0099**, 509–516.
12 S. Khodaparast, M. K. Kim, J. E. Silpe and H. A. Stone, *Environ. Sci. Technol.*, 2017, **51**, 1340–1347.
13 S. Kim, A. Greene, S. Sankaran and A. Sackner, *J. Appl. Phisiology*, 1986, **60**, 908–917.
14 L. Yang, Y. Shi, M. Abolhasani and K. F. Jensen, *Lab Chip*, 2015, **15**, 3232–3241.
15 J. Yue, E. V Rebrov and J. C. Schouten, *Lab Chip*, 2014, **14**, 1632–1649.
16 J. R. Thome, *Heat Transf. Eng.*, 2006, **27**, 4–19.
17 S. G. Kandlikar, *J. Heat Transfer*, 2012, **134**, 34001.
18 T. Harirchian and S. V Garimella, *Int. J. Heat Mass Transf.*, 2012, **55**, 1246–1260.
19 J. R. Thome, V. Dupont and A. M. Jacobi, *Int. J. Heat Mass Transf.*, 2004, **47**, 3375–3385.
20 W. B. Kolb and R. L. Cerro, *Chem. Eng. Sci.*, 1991, **46**, 2181–2195.
21 A. Polynkin, J. F. T. Pittman and J. Sienz, *Chem. Eng. Sci.*, 2005, **60**, 1591–1602.
22 F. Fairbrother and A. E. Stubbs, *J. Chem. Soc.*, 1935, **0**, 527–529.
23 G. I. Taylor, *J. Fluid Mech.*, 1960, **9**, 161–165.
24 F. P. Bretherton, *J. Fluid Mech.*, 1961, **10**, 166–188.
25 J. Ratulowski and H. C. Chang, *J. Fluid Mech.*, 1990, **210**, 303–328.
26 H. Wong, C. J. Radke and S. Morris, *J. Fluid Mech.*, 1995, **292**, 71–94.
27 A. Oron, S. H. Davis and S. G. Bankoff, *Rev. Mod. Phys.*, 1997, **69**, 931–980.
28 P. Tabeling, G. Zocchi and A. Libchaber, *J. Fluid Mech.*, 1977, **39**, 84–90.
29 Y. Han and N. Shikazono, *Int. J. Heat Fluid Flow*, 2010, **31**, 630–639.
30 D. Schubring, A. C. Ashwood, T. A. Shedd and E. T. Hurlburt, *Int. J. Multiph. Flow*, 2010, **36**, 815–824.
31 Y. Han, N. Shikazono and N. Kasagi, *Int. J. Multiph. Flow*, 2011, **37**, 36–45.
32 H. Chen, Q. Meng and J. Li, *Appl. Phys. Lett.*, 2015, **107**, 141608.
33 L. Zhang, J. Koo, L. Jiang, M. Asheghi, K. E. Goodson, J. G.

Santiago and T. W. Kenny, *J. Microelectromechanical Syst.*, 2002, **11**, 12–19.

34 S. Basu, B. Werneke, Y. Peles and M. K. Jensen, *Int. J. Heat Mass Transf.*, 2015, **91**, 1078–1087.

35 S. R. Rao, F. Houshmand and Y. Peles, *Int. J. Heat Mass Transf.*, 2014, **76**, 317–329.

36 S. Bigham and S. Moghaddam, *Int. J. Heat Mass Transf.*, 2015, **88**, 111–121.

37 S. Bigham, A. Fazeli and S. Moghaddam, *Sci. Rep.*, 2017, **7**, 44745.

38 P. Aussillous and D. Quere, *Phys. Fluids*, 2000, **12**, 2367–2371.

39 E. Klaseboer, R. Gupta and R. Manica, *Phys. Fluids*, 2014, **26**, 032107.

40 A. Cherukumudi, E. Klaseboer, S. A. Khan and R. Manica, *Microfluid. Nanofluidics*, 2015, **19**, 1221–1233.

41 A. L. Hazel and M. Heil, *J. Fluid Mech.*, 2002, **470**, 91–114.

42 A. De Lózar, A. Juel and A. L. Hazel, *J. Fluid Mech.*, 2008, **614**, 173–195.

43 A. De Lózar, A. L. Hazel and A. Juel, *Phys. Rev. Lett.*, 2007, **99**, 234501.